



UNIVERSITY OF LEEDS

This is a repository copy of *Numerical modelling for rain wind induced vibration of cables with longitudinal ribs*.

White Rose Research Online URL for this paper:
<http://eprints.whiterose.ac.uk/131431/>

Version: Accepted Version

Article:

Bi, JH, Qiao, HY, Nikitas, N orcid.org/0000-0002-6243-052X et al. (3 more authors) (2018) Numerical modelling for rain wind induced vibration of cables with longitudinal ribs. *Journal of Wind Engineering and Industrial Aerodynamics*, 178. p. 69. ISSN 0167-6105

<https://doi.org/10.1016/j.jweia.2018.05.002>

(c) 2018, Elsevier Ltd. This manuscript version is made available under the CC BY-NC-ND 4.0 license <https://creativecommons.org/licenses/by-nc-nd/4.0/>

Reuse

This article is distributed under the terms of the Creative Commons Attribution-NonCommercial-NoDerivs (CC BY-NC-ND) licence. This licence only allows you to download this work and share it with others as long as you credit the authors, but you can't change the article in any way or use it commercially. More information and the full terms of the licence here: <https://creativecommons.org/licenses/>

Takedown

If you consider content in White Rose Research Online to be in breach of UK law, please notify us by emailing eprints@whiterose.ac.uk including the URL of the record and the reason for the withdrawal request.



eprints@whiterose.ac.uk
<https://eprints.whiterose.ac.uk/>

Theory and numerical analysis on cable with ribs subject to wind and rain

J. H. Bi^{a,b,1}, H. Y. Qiao^a, N. Nikitas^c, J. Guan^a, J. Wang^{d,e}, P. Lu^f

^a School of Civil Engineering, Tianjin University, Tianjin 300350, China

^b Key Laboratory of Coast Civil Structure Safety (Tianjin University), Ministry of Education, Tianjin 300350, China

^c School of Civil Engineering, Leeds University, Leeds, UK

^d School of Civil Engineering, Tianjin Chengjian University, Tianjin 300384, China

^e Key Laboratory of Soft Soil Characteristic and Engineering Environment of Tianjin, Tianjin 300384, China

^f Central Research Institute of Building and Construction CO., LTD., MCC, Beijing 100072, China

Abstract

Aerodynamic countermeasures are among the most effective ways to mitigate rain-wind induced vibrations. However, their vibration control mechanism is in many cases still unclear. This paper presents a numerical model for a cable section with an arbitrary 2D shape, able to geometrically describe aerodynamic countermeasures, excited by both wind and rain. Based on lubrication and vibration theory, 2D coupled equations for the water film evolution and for the across wind cable vibration are derived. Wind pressure and friction coefficients, for the different evolving water-film morphologies, are calculated by CFD software, while the instantaneous water film distribution and the vibration of the cable are calculated by numerically solving the derived coupled equations. For the case of rib additions to a nominally circular cable, the model shows that there is direct impact on the formation and dynamic characteristics of the critical for rain-wind induced vibrations upper rivulet. Particularly, depending on the rib number and position(s), the countermeasure can become effective or not by altering the aeroelastic lift acting upon the cable, and redistributing its frequency content associated with instability phenomena.

Keywords: Rain-wind induced vibrations; Vibration mitigation; Stay cables; Rivulet; Lubrication theory; Aerodynamic countermeasures

Funding: This work was supported by the Natural Science Foundation of China [grant numbers 51408399];

1. Introduction

On rainy and windy days, cable-stayed bridges, with cables inclined within a certain range of angles to the wind, may experience low frequency and large amplitude vibrations; this phenomenon is broadly described with the term rain-wind induced vibrations (RWIVs). Since the phenomenon was first properly framed by Hikami and Shiraishi in 1988 (Hikami and Shiraishi, 1988), RWIVs have been the focus of a considerable volume of research. Nowadays, RWIVs are considered a serious threat to the structural integrity of cable-stayed bridges because of the large stress amplitudes they impose on cables, and particularly their supports, with clear fatigue implications that could well result to failures and substantial economic losses due to traffic closures (Li et al., 2006; Gu et al., 2007).

Researchers, through time, have proposed a series of effective countermeasures to mitigate rain-wind linked vibrations of cables. These are typically divided into three types, aerodynamic countermeasures (Flamand, 1995; Gu et al., 2005; Li et al., 2005; Kleissl and Georgakis, 2011; Li et al., 2013), structural countermeasures (Wei and Yang, 2000; Caracoglia and Jones, 2005; Bosch and Park, 2005; Caracoglia and Jones, 2007; Caracoglia and Zuo, 2009; Ahmand et al., 2015; Zhou et al., 2015) and mechanical countermeasures (Krenk, 2000; Main and Jones, 2003; Chen, 2005; Casciati and Ubertini, 2008; Cheng et al., 2010; Boston et al., 2011; Fournier and Cheng, 2014; Egger et al., 2016; Raftoyiannis and Michaltsos, 2016). Because of the advantages of low cost and easy maintenance, aerodynamic

Commented [NN1]: So the whole literature should not for instance refer to Vortex related countermeasures

countermeasures are currently popular in cable-stayed bridges all over the world; famous examples are the cases of the Sutong Bridge in China, the Normandy Bridge in France, the Cooper River Bridge in USA, the Rion-Antirion Bridge in Greece and many others. Aerodynamic countermeasures consist of cable additions like helixes, longitudinal grooves, protuberances and other similar flow spoilers. It has been broadly accepted that it is the appearance and oscillation of an upper, with respect to the flow, rivulet that drives the associated vibration phenomenon. As such, for an aerodynamic measure, the rationale to make it effective in its vibration mitigation role, is to alter the surface and shape of the cable in order to inhibit the appearance and block the oscillation of any upper rivulets. Many experimental researches and numerical simulations have been conducted to fully characterize the mitigation mechanism for different aerodynamic countermeasures. Flamand (1995) analyzed the vibration control effect of longitudinal ribs and helixes, and concluded that the function of them was to reduce the correlation between rivulets and the wind flow. Wind tunnel experiments by Gu et al. (2005) established that only helixes with certain diameter, height and twining direction characteristics could restrain RWIVs effectively. Li et al. (2005) introduced the equivalent damping ratio, as in aerodynamic damping, to quantitatively evaluate the effects of aerodynamic countermeasures in RWIV resisting performance, presenting also through wind tunnel experiments that such damping contributions are more substantial for the case of longitudinal ribs and helixes than for that of elliptical rings. An extensive wind-tunnel test campaign by Kleissl and Georgakis (2011), considering many different novel shape options, showed that shrouds had a stabilizing effect when added to a circular cylinder, while at the same time they could significantly also reduce vortex-induced oscillating lift forces; morphologies like that of a wavy, longitudinally, cylinder and a hexagonally faceted cylinder were shown to be unstable, at least for the specific geometric details selected. Li et al. (2013, 2014) investigated the effects of parameters of helical lines on RWIV control employing initially wind tunnel tests and numerically analyzing the end result of variations in terms of the mean drag coefficient, the fluctuating lift coefficient, the vortex shedding frequency, and the correlation coefficient along the cable axis.

Clearly, the majority of researchers that study rain-wind aerodynamic countermeasures, do so by mainly using wind tunnel experiments, which are extremely difficult to accurately reproduce the evolution of the water film around a tested cable. However, combining with full-scale observations, it is effectively captured that it is always the formation of rivulets that drive any dynamic instability mechanism (Verwiebe and Ruscheweyh, 1998; Peil and Nahrath, 2003; Gu and Du, 2005). Having said that, the detailed complex interactions between the external coupled rain-wind flow, the evolution of the water film and the vibration of the cable is not always unique, and there is no consensus on best selection of aerodynamic countermeasures. This makes any relevant design process rather heuristic and sometimes uncertain for engineers that need to take decisions on a one-to-one basis, supported by explicit tests. Therefore, it seems necessary to complement the field with more theoretical researches that could support developing numerical simulation tools able to capture the vibration control actions of aerodynamic countermeasures and to rationalize design.

In this paper, a new model based on lubrication theory (Lemaitre et al., 2006 and 2007), is presented in Section 2 to describe the evolution of the water film around a rain-wind exposed stay cable with an arbitrary 2D cross-sectional shape. Namely, 2D coupled equations governing the across wind motion of the cable and its water film development are derived. As means of validation, numerical results for the case of a nominally circular section cable are compared against wind tunnel dynamic test data in Section 3. In Section 4, the results of water film evolution and vibration for a stay cable equipped with different setups of longitudinal ribs are presented and analyzed in order to elucidate the vibration control mechanism of rib-like aerodynamic countermeasures.

2. Theoretical Lubrication Model

This part initially presents the kinematics of a thin water film that covers the surface of an inclined cable with an arbitrary cross-sectional shape. Subsequently, 2D coupled equations for the water film evolution and the cable

Commented [NN2]: Need the references for each

Commented [NN3]: Need the references for each (or 1 reference stating this as such)

vibration are established by combining lubrication theory and vibration theory for single-degree-of-freedom motion (Bi et al. 2013 and 2014). The proposed extension over past similar approaches, allows particularly the equations of water film evolution to be able to capture more generic morphologies of cables as is the case of aerodynamic countermeasures.

2.1 Evolution equation for the water film

As shown in Fig. 1(a), under the action of gravity \mathbf{g} and horizontal wind U_0 , a generically inclined cable covered by a water film of thickness $h(\theta, t)$ is assumed. The inclination angle α ($0^\circ \leq \alpha \leq 90^\circ$) and yaw angle β ($0^\circ \leq \beta \leq 90^\circ$) fully capture the geometry of the problem. Namely, the two also define the angle between the gravity normal \mathbf{g}_N and the wind-cable normal velocity \mathbf{U}_N vectors; this is noted as $\delta + \pi/2$, where $\delta = \arctan(\sin \alpha \cdot \tan \beta)$; see e.g. Bi et al. 2013.

The A-A cross-section of the stay cable, shown in Fig. 1(b), is taken as the object of this study. The distance $s(\theta)$ between the nominal centre and the surface of the cable is not a constant with R being the designation for the minimum value of $s(\theta)$. The gravity component along the cable and any other influence of axial flow is neglected.

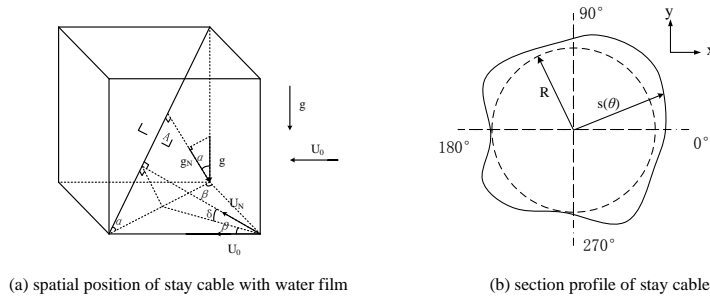


Fig. 1. Model of stay cable.

According to the lubrication theory, the equation of water film is derived by the Navier-Stokes equations written as

$$\begin{cases} \rho \frac{D\mathbf{u}}{Dt} = \rho(\mathbf{g}_N - \mathbf{a}) - \nabla p + \mu \Delta \mathbf{u} \\ \nabla \cdot \mathbf{u} = 0 \end{cases} \quad (1)$$

The velocity vector field \mathbf{u} , water density ρ , pressure P and dynamic viscosity μ of the water film are as denoted by Lemaitre et al., (2007). The vector of velocity is decomposed into $\mathbf{u} = u_r \mathbf{e}_r + u_\theta \mathbf{e}_\theta$, and in the same way we proceed for $\mathbf{g}_N = g_N^r \mathbf{e}_r + g_N^\theta \mathbf{e}_\theta$ and $\mathbf{a} = a_r \mathbf{e}_r + a_\theta \mathbf{e}_\theta$, where \mathbf{a} is the vector of acceleration of the cable in the across wind direction. $(\mathbf{e}_r, \mathbf{e}_\theta)$ stands for the pair of unit vectors in the polar coordinate system, with the water film being bounded between the $s(\theta) = r$ and the $s(\theta) + h(\theta, t) = r$ curves (i.e. instantaneous water thickness and radius variable designated by $h(\theta, t)$ and r respectively). In polar coordinates the Navier-Stokes equations take the form

$$\rho \left(\partial_t u_r + u_r \partial_r u_r + \frac{u_\theta}{r} \partial_\theta u_r - \frac{u_\theta^2}{r} \right) = \rho \left(g_N^r - a_r \right) - \partial_r p + \mu \left(\Delta u_r - \frac{2}{r^2} \partial_\theta u_\theta - \frac{u_r}{r^2} \right) \quad (2)$$

$$\rho \left(\partial_t u_\theta + u_r \partial_r u_\theta + \frac{u_\theta}{r} \partial_\theta u_r - \frac{u_r u_\theta}{r} \right) = \rho \left(g_N^\theta - \frac{\rho}{\rho} \right) - \frac{1}{r} \partial_\theta P + \mu \left(\Delta u_r + \frac{2}{r^2} \partial_\theta u_r - \frac{u_\theta}{r^2} \right) \quad (3)$$

$$\frac{1}{r} \partial_r (r u_r) + \frac{1}{r} \partial_\theta u_\theta = 0 \quad (4)$$

Dimensionless variables are defined as

$$U = \frac{R}{\nu} u_r, \quad V = \frac{R}{\nu} u_\theta, \quad P = \frac{h_0^3}{\rho \nu^2 R} p, \quad G = \frac{h_0^3}{3\nu^2} g_N, \quad (5)$$

$$\frac{r-R}{h_0} = \xi, \quad \varepsilon = \frac{h_0}{R}, \quad \zeta = \frac{r-R}{h_0} \quad (5)$$

where h_0 is the initial thickness of water film around the cable, and ν is the kinematic viscosity of the water film.

Employing these, Eqs. (2) - (4) are written in their equivalent non-dimensional form as

$$\varepsilon^3 \left[\partial_r U + U \partial_\xi U + \frac{V}{1+\varepsilon\xi} \partial_\theta U - \frac{V^2}{\varepsilon(1+\varepsilon\xi)} \right] = -3\varepsilon [G \sin(\theta-\delta) - \frac{V}{\varepsilon} \sin \theta] - \partial_\xi P \quad (6)$$

$$+\varepsilon^2 \partial_\xi \left\{ \frac{\partial_\xi [(1+\varepsilon\xi)V]}{1+\varepsilon\xi} \right\} + \frac{\varepsilon^4}{(1+\varepsilon\xi)^2} \partial_\theta^2 U - \frac{2\varepsilon^3}{(1+\varepsilon\xi)^2} \partial_\theta V$$

$$\varepsilon \left[\partial_r V + U \partial_\xi V + \frac{V}{1+\varepsilon\xi} \partial_\theta V - \frac{\varepsilon UV}{1+\varepsilon\xi} \right] = -3 [G \cos(\theta-\delta) - \frac{V}{\varepsilon} \cos \theta] - \frac{1}{1+\varepsilon\xi} \partial_\theta P \quad (7)$$

$$+\partial_\xi \left\{ \frac{\partial_\xi [(1+\varepsilon\xi)V]}{1+\varepsilon\xi} \right\} + \frac{\varepsilon^2}{(1+\varepsilon\xi)^2} \partial_\theta^2 V - \frac{2\varepsilon^3}{(1+\varepsilon\xi)^2} \partial_\theta U$$

$$\partial_\xi [(1+\varepsilon\xi)U] + \partial_\theta V = 0 \quad (8)$$

Neglecting any high order ε terms (i.e. thin-film assumption), Eqs. (6) - (8) become

$$\partial_\xi P = 0 \quad (9)$$

$$-3G \cos(\theta-\delta) + 3 \frac{V}{\varepsilon} \cos \theta - \partial_\theta P + \partial_\xi^2 V = 0 \quad (10)$$

$$\partial_\xi U + \partial_\theta V = 0 \quad (11)$$

Eqs. (9) - (11) are subject to the no-slip conditions at the cable surface

$$u_r = u_\theta = 0 \quad \text{on} \quad r = s(\theta) \quad (12)$$

and at the water-air interface, to the kinematic condition

$$u_r = \frac{Dr}{Dt} = \partial_t h + \frac{u_\theta}{r} \partial_\theta (h+s) \quad \text{on} \quad r = s(\theta) + h(\theta, t) \quad (13)$$

the normal stress condition

$$\mathbf{n}_1 \cdot (\boldsymbol{\sigma}_g - \boldsymbol{\sigma}) \cdot \mathbf{n}_1 = \kappa \gamma \quad \text{on } r = s(\theta) + h(\theta, t) \quad (14)$$

and the tangential stress condition

$$\mathbf{t}_1 \cdot (\boldsymbol{\sigma}_g - \boldsymbol{\sigma}) \cdot \mathbf{n}_1 = 0 \quad \text{on } r = s(\theta) + h(\theta, t) \quad (15)$$

where $\boldsymbol{\sigma}_g$ and $\boldsymbol{\sigma}$ are the stress tensors of air and water respectively, at the interface of water film and air, γ is the coefficient of surface tension and κ is the curvature of the free surface, given by

$$\kappa = \nabla \cdot \mathbf{n}_1 = \frac{(s+h)^2 + 2[\partial_\theta(s+h)]^2 - (s+h)\partial_\theta^2(s+h)}{\left\{ (s+h)^2 + [\partial_\theta(s+h)]^2 \right\}^{\frac{3}{2}}} \quad (16)$$

The normal \mathbf{n}_1 and tangential \mathbf{t}_1 vectors are given by

$$\mathbf{n}_1 = \frac{1}{N_1} \left(\mathbf{e}_r - \frac{1}{r} \partial_\theta r \mathbf{e}_\theta \right) \quad (17)$$

$$\mathbf{t}_1 = \frac{1}{N_1} \left(\frac{1}{r} \partial_\theta r \mathbf{e}_r + \mathbf{e}_\theta \right) \quad (18)$$

$$\text{with } N_1 = \sqrt{1 + \frac{1}{r^2} (\partial_\theta r)^2} \quad (19)$$

The normal and tangential stress conditions of Eq. (14) and Eq. (15) expressed in polar coordinates become

$$-p_g + p - \frac{2\mu}{N_1^2 r} \left\{ (u_r + \partial_\theta u_\theta) \left[\left(\frac{1}{r} \partial_\theta r \right)^2 - 1 \right] - \partial_\theta r \left[r \partial_\theta \left(\frac{u_\theta}{r} \right) + \frac{1}{r} \partial_\theta u_r \right] \right\} - \frac{2\boldsymbol{\tau}_g}{N_1^2 r} \partial_\theta h = \frac{\gamma}{N_1^3} \left[\frac{1}{r} + \frac{2}{r^3} (\partial_\theta r)^2 - \frac{1}{r^2} \partial_\theta^2 r \right] \quad (20)$$

$$\mathbf{t}_1 \cdot \boldsymbol{\sigma}_g \cdot \mathbf{n}_1 - \frac{\mu}{N_1^2} \left\{ -\frac{4}{r^2} \partial_\theta r (u_r + \partial_\theta u_\theta) + \left[1 - \left(\frac{1}{r} \partial_\theta r \right)^2 \right] \left[r \partial_\theta \left(\frac{u_\theta}{r} \right) + \frac{1}{r} \partial_\theta u_r \right] \right\} = 0 \quad (21)$$

The following dimensionless numbers need to appear within the boundary conditions

$$P = \frac{\rho_g U_N^2 h_0^3}{6\rho \nu^2 R}, \quad \mathbf{T}_g = \frac{h_0^3}{\rho \nu^2 R} \boldsymbol{\tau}_g, \quad C = \varepsilon^3 \frac{h_0 \gamma}{3\rho \nu^2}, \quad C_p = \frac{p_g}{\frac{1}{2} \rho_g U_N^2}, \quad C_r = \frac{\mathbf{t}_1 \cdot \boldsymbol{\sigma}_g \cdot \mathbf{n}_1}{\frac{1}{2} \rho_g U_N^2}, \quad (22)$$

$$S = \frac{s}{R}, \quad K = \kappa \cdot R, \quad T = \frac{\nu}{R h_0} t, \quad H = \frac{h}{h_0}.$$

where ρ_g is the air density, $\boldsymbol{\tau}_g$ is the viscous stress tensor of air, and p_g is the air pressure at the air - water film interface.

When the dimensionless numbers defined in Eq. (22) are substituted into Eqs. (12) - (13), and Eqs. (20) - (21),

the modified boundary conditions are written as

$$(A = \frac{S-1}{\varepsilon}, B = \frac{S-1}{\varepsilon} + H)$$

$$U|_{\xi=A} = V|_{\xi=A} = 0 \quad (23)$$

$$U = \partial_T H + \frac{V}{S} \partial_\theta H + \left(\frac{1}{\varepsilon} - \frac{H}{S}\right) \frac{V}{S} \partial_\theta S \quad (24)$$

$$-3PC_p + P = \frac{3CK}{\varepsilon} \quad (25)$$

$$3\frac{P}{\varepsilon} C_f - \frac{1}{N_1^2} \left[S - \frac{1}{S} (\partial_\theta S)^2 \right] \partial_\xi V|_{\xi=B} = 0 \quad (26)$$

The dimensionless form of the boundary conditions Eqs. (23) - (26) are substituted into the equivalent Navier-Stokes equations, Eqs. (9) - (11), to finally obtain

$$\begin{aligned} \partial_T H + \left[\frac{\partial_\theta S + \varepsilon \partial_\theta H}{\varepsilon(S + \varepsilon H)} - \frac{1}{\varepsilon} \partial_\theta S - \partial_\theta H \right] & \left\{ -\frac{3}{2} \left[G \cos(\theta - \delta) - \frac{C}{\varepsilon} \cos \theta + P \partial_\theta C_p + \frac{C}{\varepsilon} \partial_\theta K \right] H^2 + \frac{3PC_f N_1^2}{\varepsilon \left[S - \frac{1}{S} (\partial_\theta S)^2 \right]} H \right\} \\ + \partial_\theta & \left\{ \left[-G \cos(\theta - \delta) + \frac{C}{\varepsilon} \cos \theta - P \partial_\theta C_p - \frac{C}{\varepsilon} \partial_\theta K \right] H^3 + \frac{3PC_f N_1^2}{2\varepsilon \left[S - \frac{1}{S} (\partial_\theta S)^2 \right]} H^2 \right\} = 0 \end{aligned} \quad (27)$$

Eq. (27) is the evolution equation for the water film when this rests on a cable with arbitrary section. For $s(\theta) = R$, $S = 1$, the equation is used for a cable with 2D circular cross-sectional shape. Eq. (27) agrees with the earlier equations given by Bi et al. (2013) for the special case of a circular cylinder and with these of Lemaitre et al. (2007) and Robertson et al. (2010) for the case the cylinder is also stationary.

2.2. Motion equation of cable

The across wind motion equation of a single-degree-of-freedom equivalent stay cable is given by

$$\ddot{y} + 2\omega_0 \xi_0 \dot{y} + \omega_0^2 y - \frac{1}{M} F_y = 0 \quad (28)$$

where ω_0 , ξ_0 , M , F_y are the circular natural frequency, damping ratio, mass and lift of the cable respectively,

$$F_y = \int_0^{2\pi} [F_r(\theta) \sin \theta + F_\theta(\theta) \cos \theta] d\theta, \quad F_r(\theta) \quad \text{and} \quad F_\theta(\theta)$$

are the normal and tangential forces of water film bottom ($r = s(\theta)$).

The stress tensor σ_0 of the water at the water film – cable interface is

$$\boldsymbol{\sigma}_0 = \left\{ -p\mathbf{I} + \mu \left[\nabla \mathbf{u} + (\nabla \mathbf{u})^T \right] \right\} \Big|_{r=R} = \left[\begin{array}{cc} -p + 2\mu \partial_r u_r & \mu \left(\partial_r u_\theta + \frac{\partial_\theta u_r}{r} - \frac{u_\theta}{r} \right) \\ \mu \left(\partial_r u_\theta + \frac{\partial_\theta u_r}{r} - \frac{u_\theta}{r} \right) & -p + 2\mu \left(\frac{\partial_\theta u_\theta}{r} + \frac{u_r}{r} \right) \end{array} \right] \Big|_{r=S} \quad (29)$$

The normal \mathbf{n}_2 and tangential \mathbf{t}_2 vectors at the bottom of the water film (i.e. cable-surface) are given by

$$\mathbf{n}_2 = \frac{1}{N_2} \left(\mathbf{e}_r - \frac{1}{s} \partial_\theta s \mathbf{e}_\theta \right) \quad (30)$$

$$\mathbf{t}_2 = \frac{1}{N_2} \left(\frac{1}{s} \partial_\theta s \mathbf{e}_r + \mathbf{e}_\theta \right) \quad (31)$$

$$\text{with } N_2 = \sqrt{1 + \frac{1}{s^2} (\partial_\theta s)^2} \quad (32)$$

Then we obtain

$$F_r(\theta) = \mathbf{e}_r \cdot \boldsymbol{\sigma}_0 \cdot \mathbf{n}_2 = \left[\frac{1}{N_2} (-p + 2\mu \partial_r u_r) - \frac{\mu \partial_\theta s}{N_2 s} \left(\partial_r u_\theta + \frac{\partial_\theta u_r}{r} - \frac{u_\theta}{r} \right) \right] \Big|_{r=S} \quad (33)$$

$$F_\theta(\theta) = \mathbf{e}_\theta \cdot \boldsymbol{\sigma}_0 \cdot \mathbf{n}_2 = \left[\frac{\mu}{N_2} \left(\partial_r u_\theta + \frac{\partial_\theta u_r}{r} - \frac{u_\theta}{r} \right) - \frac{\partial_\theta s}{N_2 s} (-p + 2\mu \frac{\partial_\theta u_\theta}{r} + 2\mu \frac{u_r}{r}) \right] \Big|_{r=S} \quad (34)$$

The dimensionless forms of $F_r(\theta)$ and $F_\theta(\theta)$ are given by

$$\chi_r(\theta) = \frac{h_0^2}{\rho v^2} F_r(\theta) = \left[\frac{h_0^2}{N_2 s} \left(-\frac{p}{\mu} + 2\partial_r u_r \right) - h_0^2 \frac{\partial_\theta s}{N_2 s v} \left(\partial_r u_\theta + \frac{\partial_\theta u_r}{r} - \frac{u_\theta}{r} \right) \right] \Big|_{r=S} \quad (35)$$

$$\chi_\theta(\theta) = \frac{h_0^2}{\rho v^2} F_\theta(\theta) = \left[\frac{h_0^2}{N_2 s} \left(\partial_r u_\theta + \frac{\partial_\theta u_r}{r} - \frac{u_\theta}{r} \right) - h_0^2 \frac{\partial_\theta s}{N_2 s v} \left(-\frac{p}{\mu} + 2\frac{\partial_\theta u_\theta}{r} + 2\frac{u_r}{r} \right) \right] \Big|_{r=S} \quad (36)$$

Using the rest of the dimensionless numbers defined in Eq. (5), Eqs. (35) - (36) become

$$\begin{aligned} \chi_r(\theta) &= \left\{ \frac{1}{N_2} \left(-\frac{R}{h_0} P + \frac{2h_0}{R} \partial_\xi U \right) - \frac{\partial_\theta S}{N_2 S} \left[\partial_\xi V + \frac{h_0^2 \partial_\theta U}{R(\xi h_0 + R)} - \frac{v h_0}{\xi h_0 + R} \right] \right\} \Big|_{\xi=A} \\ &= -\frac{1}{N_2 \varepsilon} \left(\frac{3CK}{\varepsilon} + 3PC_p \right) + \left[\frac{2}{N_2} \partial_\theta S - \frac{\partial_\theta S}{N_2 S} + \frac{(\partial_\theta S)^3}{N_2 S^2} \right] \left\{ \frac{3PC_f N_1^2}{\varepsilon \left[S - \frac{1}{S} (\partial_\theta S)^2 \right]} - 3[G \cos(\theta - \delta) - \frac{R}{S} \cos \theta + P \partial_\theta C_p \right. \\ &\quad \left. + \frac{C}{\varepsilon} \partial_\theta K \right\} H \end{aligned} \quad (37)$$

$$\begin{aligned}
\chi_\theta(\theta) &= \left\{ \frac{1}{N_2} \left[\partial_\xi V + \frac{h_0^2 \partial_\theta U}{R(\xi h_0 + R)} - \frac{h_0 V}{\xi h_0 + R} \right] - \frac{\partial_\theta S}{N_2 S} \left[-\frac{R}{h_0} P + \frac{2h_0 \partial_\theta V}{\xi h_0 + R} + \frac{2h_0^2 U}{R(\xi h_0 + R)} \right] \right\} \Bigg|_{\xi=A} \\
&= \frac{\partial_\theta S}{N_2 S \varepsilon} \left(\frac{3CK}{\varepsilon} + 3PC_p \right) + \left[\frac{1}{N_2} - \frac{(\partial_\theta S)^2}{N_2 S} + \frac{2(\partial_\theta S)^2}{N_2 S^2} \right] \left\{ \frac{3PC_f N_1^2}{\varepsilon \left[S - \frac{1}{S} (\partial_\theta S)^2 \right]} - 3 \left[G \cos(\theta - \delta) - \frac{W}{S} \cos \theta + P \partial_\theta C_p \right. \right. \\
&\quad \left. \left. + \frac{C}{\varepsilon} \partial_\theta K \right] H \right\}
\end{aligned} \quad (38)$$

The lift of the cable can thus be expressed as

$$F_y = \frac{\rho V^2}{h_0^2} \int_0^{2\pi} [\chi_r(\theta) \sin \theta + \chi_\theta(\theta) \cos \theta] d\theta \quad (39)$$

2.3 Numerical solver and parameter selection

Wind pressure C_p and friction C_f coefficients are leading parameters within the water film evolution Eq. (27). Because of variations in the rivulet position and shape, both C_p and C_f vary with time. For their calculation the CFD software COMSOL Multiphysics, which can compute their instantaneous values and subsequently stream output to Matlab quickly, is used. Eqs. (27) - (28) are evaluated in Matlab; being fourth and second order non-linear partial differential equations respectively, a finite difference scheme using an N-point spatial discretization is employed to solve both of them. The flow chart for the numerical solution to be used is shown in Fig. 2. This is equivalent to the one of Bi et al. (2016), where the reader can get a more comprehensive description of its rationale and origins.

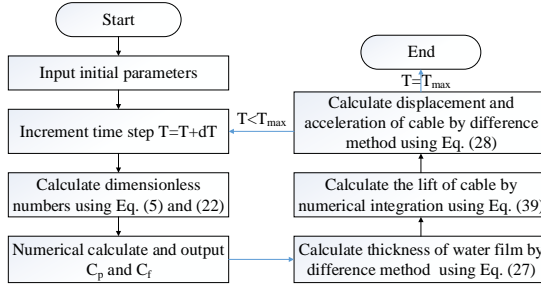


Fig. 2. Flow chart of numerical calculation scheme.

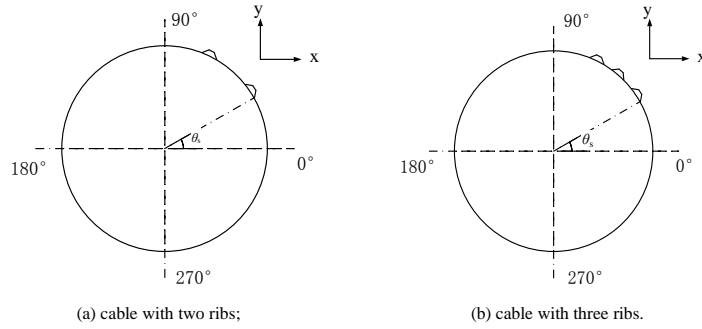
An equi-spaced distribution of $N = 128$ circumferential points and a time-step of $\Delta t = 10^{-4}$ s were chosen for the scheme. Conforming to the experiment of Li et al. (2010), the maximum rivulet thickness is set at 1.25mm. In order to keep the water film continuous, the minimum rivulet thickness is assumed as 0.02mm. The parameters of Eqs (27) - (28) are such that comply with details in the experiment of Li et al. (2010), and are listed in Table 1.

Fig. 3 shows the schematic diagram of circular section stay cable with longitudinal ribs. The height and width of the ribs are 2mm and 7.4mm, respectively. In any case, ribs are positioned on only one side that corresponds to the upper rivulet formation region, promoting though due to the asymmetry ordinary dry galloping phenomena. According to the experiment of Li et al. (2010), the oscillation range of upper rivulets is $\theta \approx 30^\circ \sim 75^\circ$. Therefore, in Fig. 3 there are two options with ribs located at $\theta_s = 30^\circ$ and $\theta_s = 60^\circ$ (close to the start and end points), (a), and another where three ribs are located at $\theta_s = 30^\circ$, $\theta_s = 45^\circ$ and $\theta_s = 60^\circ$, (b). The function $s(\theta)$ is defined via assigning the relevant 128-point values in Matlab.

Table 1

Values of parameters used in the numerical calculations.

Parameter	Value
Cable radius, R	0.05 m
Cable natural frequency, f	0.952 Hz
Cable inclination angle, α	30°
Wind yaw angle, β	22.5°
Acceleration of gravity, g	9.8 m/s^2
Density of water, ρ	10^3 kg/m^3
Kinematic viscosity of water, ν	$10^{-6} \text{ m}^2/\text{s}$
Surface tension coefficient of water in the air, γ	$7.2 \times 10^{-2} \text{ N/m}$
Density of air, ρ_g	1.225 kg/m^3
Damping ratio, ξ_0	0.17%

**Fig 3.** Section profile of studied stay cables with longitudinal ribs.

3. Model verification

For $s(\theta) = R$, $S = 1$, the model describes a cable with a perfect circular cross-sectional shape. In order to validate the proposed theoretical model and numerical procedure, numerical results are compared against the previously cited wind tunnel test data (Li et al., 2010). In the experiments of Li et al., RWIVs occurred in the wind speed region of $U_0 = 6.76\text{--}8.04 \text{ m s}^{-1}$, with substantial detail given for the case of $U_0 = 7.72 \text{ m s}^{-1}$, which is herein selected.

Fig. 4 shows the cable across wind response and its equivalent power spectrum density during $t = 0\text{--}80 \text{ s}$. Initially, the motion amplitude starts off from 0.02 m . Then it increases continuously until $t = 27 \text{ s}$, when it reaches its maximum of 0.10 m . This value is close to the wind tunnel data of 0.09 m (Li et al., 2010). The dominant motion frequency is identified at 0.99 Hz , which is also close to the experimental data of 0.95 Hz .

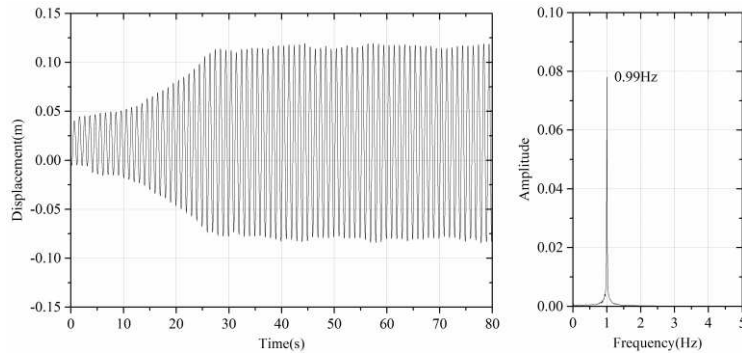


Fig. 4. Vibration response and frequency of the cable

Fig. 5 presents the evolution of the water film around the circular cable during $t = 40\text{--}80$ s. An upper rivulet formation keeps oscillating significantly, while a lower one almost maintains stable. For the former, the oscillation range is between 30° and 75° . Similar results are also observed in the wind tunnel. Further, the mean thickness of the upper rivulet is 0.49 mm which is also close to the experimentally observed 0.51 mm. In order to research the time variation of this upper rivulet, the thickness and power spectrum density of the water film at $\theta = 56.25^\circ$, this being close to the expected formation point, are shown in Fig. 6. Namely, the frequency content is primarily at the motion frequency and its higher, odd and even, harmonics, matching again observations.

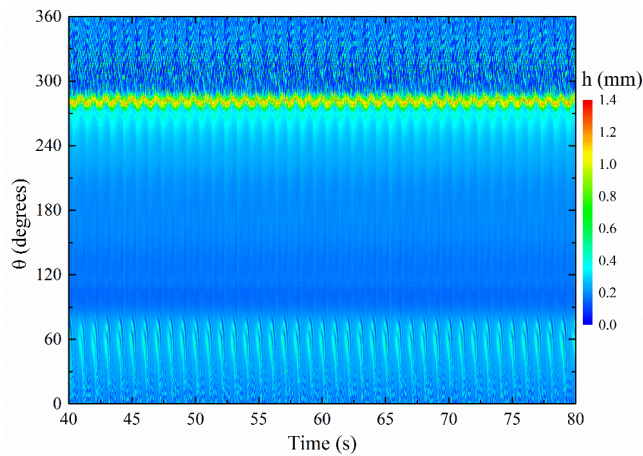


Fig. 5. Evolution of the water film around the cable

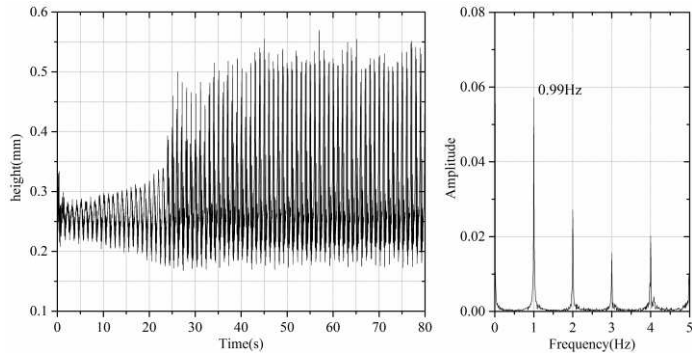


Fig. 6. Thickness and frequency of the water film at position $\theta = 56.25^\circ$

Cable lift and its associated power spectral density are presented in Fig. 7, in order to compare against cables with ribs. The lift varies between 0 and 1.3N, with a dominant frequency at 0.99Hz. Fig. 8 combines output for the water thickness at $\theta = 56.25^\circ$, the lift and the motion for $t = 50-60$ s. Although the thickness data show some spikes, all signals look synchronized between them promoting resonance and interaction phenomena.

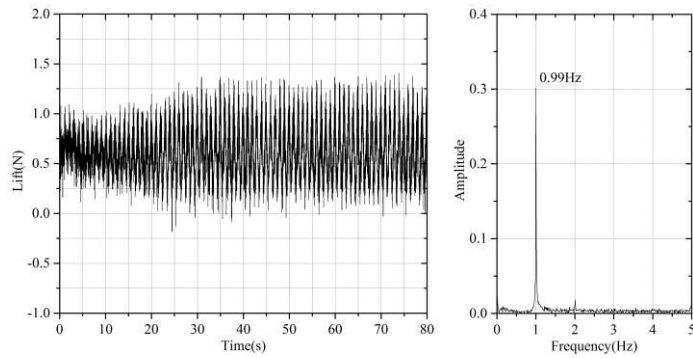


Fig. 7. Lift and frequency of the cable

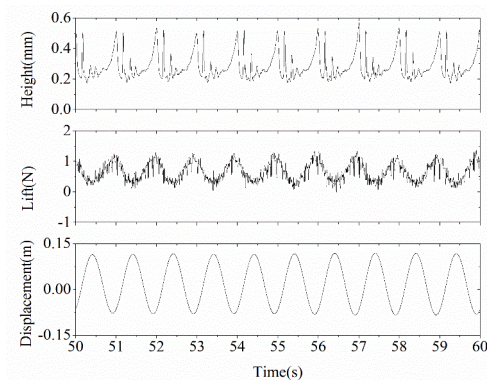


Fig. 8. Combined information for the water film, lift and oscillation of the cable

4. Results

4.1 Vibration response of cable with ribs

Compared with the case of a circular cable, the vibration response, lift and evolution of the water film for a cable with longitudinal ribs are calculated and analyzed to investigate the effect of the modified aerodynamic shape on RWIVs.

Figs. 9 and 10 show the vibration responses and frequency spectrum for cables with two and three ribs, respectively. The dominant frequency (0.97Hz), in both cases, is close to the natural frequency prescribed (0.95Hz). In Fig. 9, the amplitude keeps stable at 0.03 m, which is much lower than that of the circular cable. This means that cables with two ribs have good performance on restraining the large amplitudes RWIVs.

In Fig. 10, at the start, the amplitude of the cable is even less, 0.02 m, and gradually further decays until $t \approx 24$ s, when the cable can even be considered not moving. As such, the aerodynamic impact of three ribs is superior to that of two ribs, resulting in an over ten-fold comparative vibration reduction, at least for the wind angles considered.

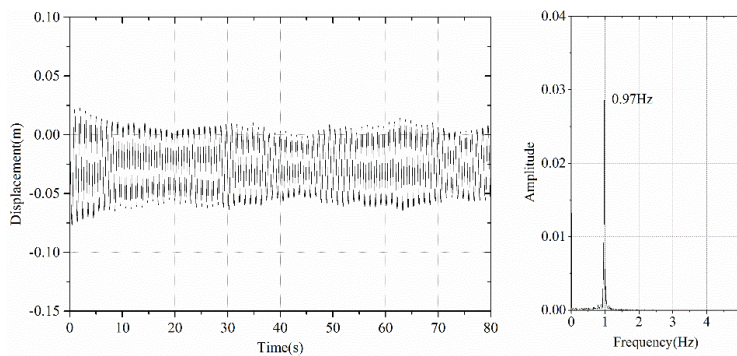


Fig. 9. Vibration response and frequency analysis of cable with two ribs

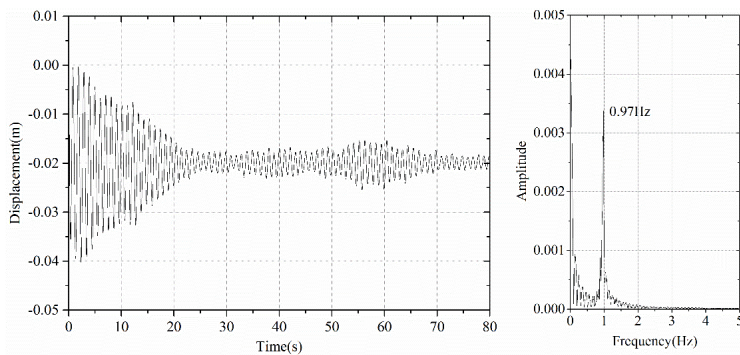


Fig. 10. Vibration response and frequency analysis of cable with three ribs

4.2 Aerodynamic lift of cable with ribs

Figs. 11 and 12 present lift and its frequency spectrum, again for cables with two and three ribs respectively. Lift

for both cases is always negative, something which agrees with the fact that the balance position of vibration in Figs. 8 and 9 are below zero. In Fig. 11, the lift varies between -1.4N and -0.6N. Although the dominant frequency (0.97Hz) is approximately equal to the specified natural frequency of the cable (0.95Hz), the energy content on the dominant frequency is much reduced compared to that of the circular cable in Fig. 7, besides, there is also considerable energy distribution below 0.97Hz. Thus the two rib cable could not vibrate at the large amplitude of the Fig. 4 case.

In Fig. 12, the lift varies between -1.1N and -0.5N, and its range is smaller than that in the case of the circular cable in Fig.7. The lift oscillations at higher frequencies, 11.88Hz, 23.76Hz and 35.64Hz, are clearly connected to vortex shedding. This may be the reason why the resonance phenomenon of cable does not appear, and the vibration amplitude of cable almost gradually decays to zero.

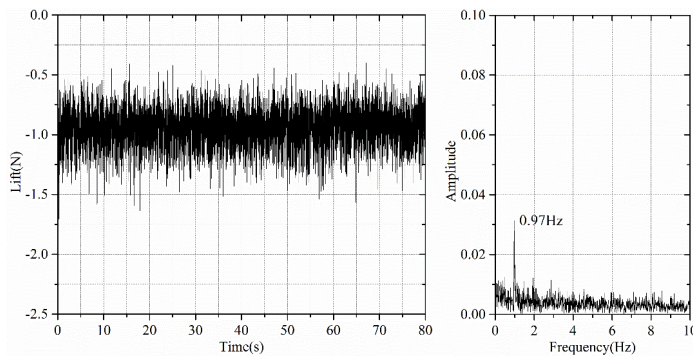


Fig. 11. Aerodynamic lift and frequency analysis of cable with two ribs

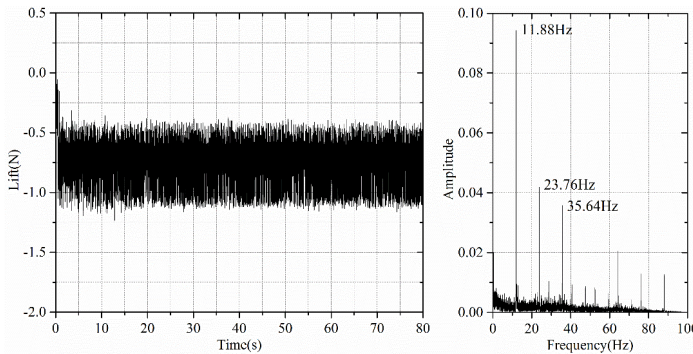


Fig. 12. Aerodynamic lift and frequency analysis of cable with three ribs

4.3 Evolution of water film around cable with ribs

Figs. 13 and 14 show the evolution of water film around cable with two and three ribs, respectively. In Fig. 13, lower rivulet is formed at $\theta \approx 278.4^\circ$ and oscillates between $\theta \approx 275.6^\circ$ and $\theta \approx 286.9^\circ$, the average height and width are 1.25mm and 2.62mm, respectively. Located in the oscillation range of upper rivulet, the two ribs have an effect on the formation and oscillation of upper rivulet. Although there exists three evident upper rivulets between the two ribs, unlike the rivulet in Fig. 5, the rivulets in Fig. 13 almost do not oscillate, and the maximum height of upper rivulet is 0.43mm which is lower than that in Fig. 5. Besides, as the ribs impede water film to flow along the cable, two stationary rivulets are formed with a thickness of 1.25mm at the upper edges of the ribs, there are also a little water accumulating at the lower edges of the ribs with a thickness of 0.26mm.

In Fig. 14, the appearance of lower rivulet occurs almost at the same time comparing with the case of cable with two ribs, and lower rivulet is formed at $\theta \approx 281.3^\circ$ and oscillates between $\theta \approx 275.6^\circ$ and $\theta \approx 286.8^\circ$. The height and width are 1.25mm and 2.18mm, respectively. Unlike the cases of circular cable and cable with two ribs, there is not obvious rivulet among the three ribs. It is the ribs that prevent the formation of upper rivulet. Water film accumulates at the upper edge of the ribs with the thickness of 1.25mm, while at the lower edge of the ribs thickness of water film is only 0.23mm.

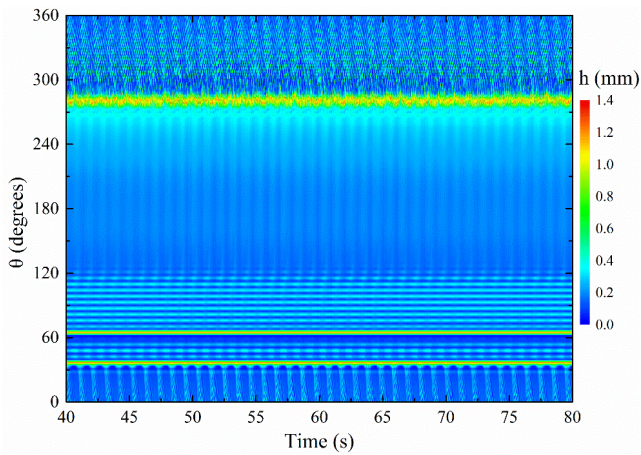


Fig. 13. Evolution of water film around cable with two ribs

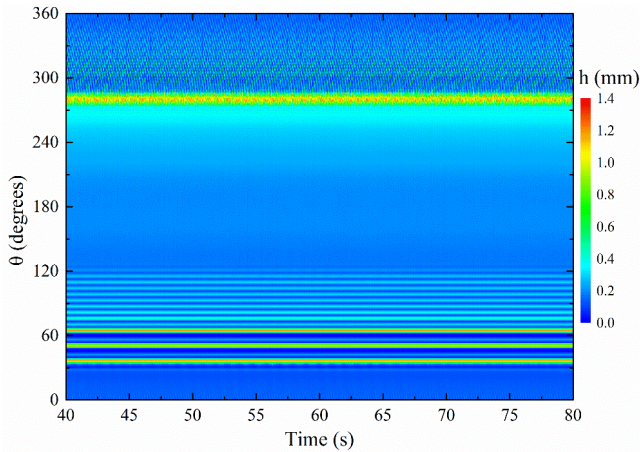


Fig. 14. Evolution of water film around cable with three ribs

In order to further investigate the evolution of water film and motion of upper rivulet, thickness of water film at $\theta = 56.25^\circ$ is selected to compare with the case of circular cable in Figs. 6, 15 and 16 show the thicknesses and frequency analysis of water film around cable with two and three ribs at the position of $\theta = 56.25^\circ$. In Fig. 15, the thickness of water film varies between 0.23mm and 0.30mm which is lower than that of the circular cable (0.52mm). There are two dominant frequencies, 0.97Hz and 13.41Hz, the dominant frequency (13.41Hz) of water film thickness

at $\theta = 56.25^\circ$ also has a bit energy.

In Fig. 16, the maximum thickness of water film is 0.035mm, which is close to vicinal water film. There is no apparent upper rivulet existing around the cable, and the dominant frequencies are 11.89Hz and 23.76Hz, which hold only a little energy. Thus the resonance between evolution of water film and vibration of cable can not occur, and the vibration amplitude of cable gradually decays to zero.

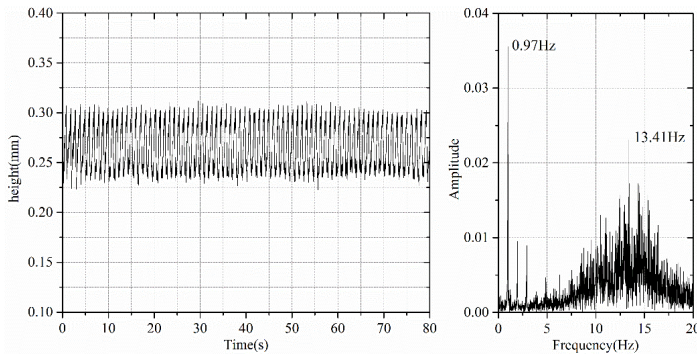


Fig. 15. Thickness and frequency analysis of water film around cable with two ribs at the position of $\theta = 56.25^\circ$

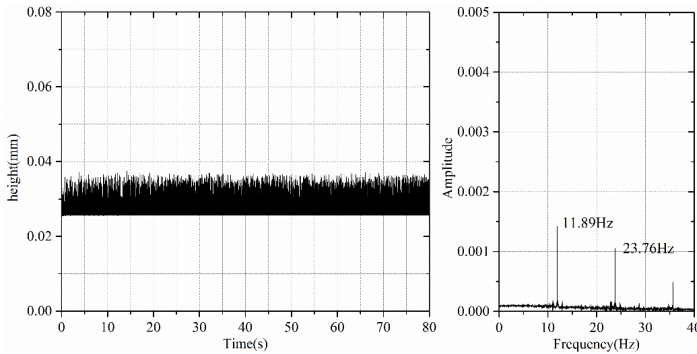


Fig. 16. Thickness and frequency analysis of water film around cable with three ribs at the position of $\theta = 56.25^\circ$

Figs. 17 and 18 show the coupling relationships among the water film thickness at $\theta = 56.25^\circ$, aerodynamic lift and vibration amplitude of cable with ribs from $t = 50s$ to $60s$. In Fig. 17, the dominant frequency of water film at $\theta = 56.25^\circ$ is comparable to the vibration frequency of the cable, however, the variation law of aerodynamic lift has no periodicity. The vibration control mechanism of cable with two ribs could be ascertained as follows: As the two ribs are located in the oscillation range of upper rivulet, some water accumulates at the upper and lower edges of the ribs rather than merge into upper rivulet. Although several upper rivulets are formed between the ribs, the thicknesses of the rivulets are much smaller than that of the circular cable. Besides, the ribs also decrease the oscillation range of upper rivulets, the interaction among the upper rivulets brings about the disorders of rivulets, thus the dominant frequency (13.41Hz) of water film thickness at the position of $\theta = 56.25^\circ$ also has a bit energy distribution. Because of the thinner upper rivulets and disorders of rivulets, the periodicity of aerodynamic lift is not very obvious, thus the amplitude of the cable is much smaller than that of the circular cable.

In Fig. 18, although the cable vibrates with natural frequency, the evolution of water film and aerodynamic lift

fluctuate with no apparent periodicity. The vibration control mechanism of cable with three ribs could be concluded as follows: Unlike the case of cable with two ribs, three ribs impede the formation of upper rivulet. Water film mainly accumulates at the upper and lower edges of the three ribs, and water film thickness at $\theta = 56.25^\circ$ fluctuates with no obvious periodicity. The aerodynamic lift also varies with no periodicity, therefore, the resonance between rivulets and cable is suppressed and the amplitude of the cable gradually decays to zero.

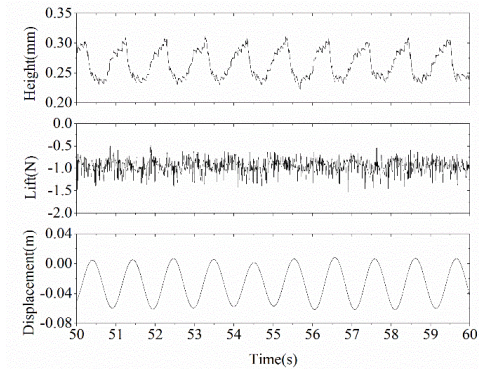


Fig. 17. Coupling relationship among water film, lift and oscillation of cable with two ribs

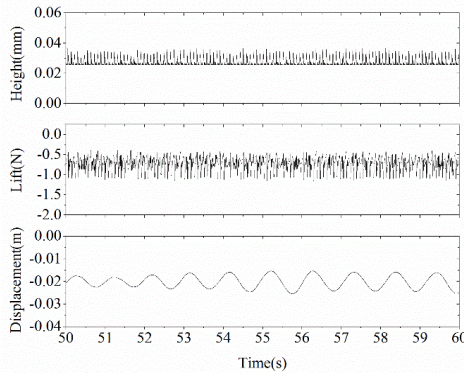


Fig. 18. Coupling relationship among water film, lift and oscillation of cable with three ribs

5. Conclusions

In this study, 2D coupled equations governing vibration of cable with an arbitrary shape and evolution of water film are both established. To analyze a possible vibration control mechanism, the vibration characteristics of the cable with longitudinal ribs, the rivulets and the aerodynamic lift are investigated by solving the coupled equations. The following conclusions can be drawn from this study:

- (1) The numerical model and solution process have been demonstrated to be accurate and effective, the investigations of circular cable are in excellent agreement with experimental results, the resonance between rivulets and cable may be one of the main reasons for RWIV.
- (2) Cable with two ribs at the position of $\theta_s=30^\circ$ and $\theta_s=60^\circ$ could not vibrate with large amplitude because the ribs have an effect on the formation and oscillation of upper rivulets. Although several upper rivulets are formed, the

thicknesses of upper rivulets are much lower than the case of circular cable. Also, the oscillation range of upper rivulets is smaller and the periodicity of upper rivulets is weaker. Thus the aerodynamic lift is smaller and has no obvious periodicity, therefore the resonance between water film and cable does not occur.

- (3) Cable with three ribs at the position of $\theta_s=30^\circ$, $\theta_s=45^\circ$ and $\theta_s=60^\circ$ respectively could not vibrate with large amplitude because the ribs impede the formation of upper rivulet, there is no apparent upper rivulet formed on cable surface. The subtle change in water film morphology could not bring about large amplitude of lift, and lift variation has no periodicity, thus cable vibration gradually decays to zero.
- (4) The RWIV control effect of cable with three ribs at the position of $\theta_s=30^\circ$, $\theta_s=45^\circ$ and $\theta_s=60^\circ$ is much better than the case of cable with two ribs at the position of $\theta_s=30^\circ$ and $\theta_s=60^\circ$. Although two ribs have an effect on the formation of upper rivulet, there are still several upper rivulets formed around the cable. While three ribs could completely hinder the formation and oscillation of upper rivulet which is the main reason of RWIV.

References

- Boston, C., Weber, F., Guzzella, L., 2011. Optimal semi-active damping of cables with bending stiffness, *Smart Materials and Structures* 20, 1-8.
- Bi, J.H., Wang, J., Shao, Q., 2013. 2D numerical analysis on evolution of water film and cable vibration response subject to wind and rain, *Journal of Wind Engineering and Industrial Aerodynamics* 121, 49-59.
- Bi, J.H., Wang, J., Shao, Q., Lu, P., 2014. Two-way coupling between water film morphology and rain-wind induced vibration of cable, *Engineering Mechanics* 7, 54-60. (in chinese).
- Bi, J.H., Wang, J., Lu P., Bao C., 2014. Variation of water film morphology and aerodynamic force of stay cable, *Journal of Tianjin University (Science and Technology)* 47, 479-490. (in chinese).
- Bi, J.H., Guan, J., Wu, J., 2016. Analysis on vibration of cable, lift and water film morphology during rain wind induced vibration. *Journal of Tianjin University (Science and Technology)*. (in chinese).
- Caracoglia, L., Jones, N.P., 2005. In-plane dynamic behaviour of cable networks part 1: formulation and basic solutions, *Journal of Sound and Vibration* 279, 969-991.
- Caracoglia, L., Jones, N.P., 2005. In-plane dynamic behavior of cable networks part 2: prototype prediction and validation, *Journal of Sound and Vibration* 279, 993-1014.
- Chen, W.L., Tang, S.R., Li, H., Hu, H., 2013. Influence of dynamic properties and position of rivulet on rain wind induced vibration of stay cables, *ASCE, Journal of Bridge Engineering*, 18(10), 1021-1031.
- Chen, Z.Q., 2005. Field observation and vibration control of rain wind induced vibration of stay cable, *Journal of Architecture Science and Engineering* 22, 5-19. (in chinese).
- Casciati, F., Ubertini, F., 2008. Nonlinear vibration of shallow cables with semiactive tuned mass damper, *Nonlinear Dynamics* 53, 89-106.
- Egger, P., Caracoglia, L., Kollegger, J., 2016. Modeling and experimental validation of a multiple-mass-particle impact damper for controlling stay-cable oscillations, *Structural Control and Health Monitoring* 23, 960-978.
- Gu, M., Du, X.Q., 2005. Experimental investigation of rain wind induced vibration of cables in cable-stayed bridges and its mitigation. *Journal of Wind Engineering and Industrial Aerodynamics* 93, 79-95.
- Gu, M., Du, X.Q., Li, S.Y., 2007. Experimental and theoretical study on rain wind induced vibration of cables of cable-stayed bridges. *Journal of Vibration Engineering* 20(5), 473-479. (in chinese).
- Hikami, Y., Shiraishi, N., 1988. Rain-wind induced vibrations of cables stayed bridges. *Journal of Wind Engineering*

- and *Industrial Aerodynamics* 29(1), 409-418.
- Bosch, H.R., Park S.W., 2005. Effectiveness of external dampers and cross-ties in mitigation of stay cable vibrations, *Proceedings of the 6th International Symposium on Cable Dynamics*, Charleston, South Carolina, USA, September 19–22, CD-ROM.
- Zhou, H., Yang, X., Sun, L., Xing, F., 2015. Free vibrations of a two-cable network with near-support dampers and a cross-link, *Structural Control and Health Monitoring* 22(9).
- Main, J.A., Jones, N.P., 2003. Influence of rubber bushings on stay-cable damper effectiveness, *Proceedings of the 5th International Symposium on Cable Dynamics*, Santa Margherita Ligure; Italy.
- Fournier, J., Cheng, S., 2014. Impact of damper stiffness and damper support stiffness on the efficiency of a linear viscous damper in controlling stay cable vibrations, *Journal of Bridge Engineering ASCE* 19(4) 04013022.
- Ahmad, J., Cheng, S., Ghrib, F., 2015. Effect of number of cross-tie lines on the in-plane stiffness and modal behaviour classification of orthogonal cable networks with multiple lines of transverse flexible cross-ties. *Journal of Engineering Mechanics ASCE* 142(4) 04015106.
- Ahmad, J., Cheng, S., Ghrib, F., 2016. Impact of cross-tie design on the in-plane stiffness and local mode formation of cable networks on cable-stayed bridges, *Journal of Sound and Vibration* 363 141–155.
- Kleissl, K., Georgakis, C.T., 2011. Aerodynamic control of bridge cables through shape modification: A preliminary study. *Journal of Fluids and Structures* 27, 1006-1020.
- Li, H., Chen, W.L., Xu, F., Li, F.C., 2010. A numerical and experimental hybrid approach for the investigation of aerodynamic forces on stay cables suffering from rain wind induced vibration, *Journal of Fluid and Structures*, Vol 26, No.7-8, 1195-1215.
- Li, W.B., Lin, Z.X., 2005. A study on aerodynamic control countermeasures to rain-wind induced vibration of cables in cable-stayed bridge. *China Civil Engineering Journal* 38(5), 48-53. (in chinese).
- Lemaitre, C., Alam, M.M., Hémon, P., 2006. Rainwater rivulets on a cable subject to wind, *Comptes Rendus Mécanique* 334, 158-163.
- Lemaitre, C., Hémon, P., Langre, E., 2007. Thin water film around a cable subject to Wind. *Journal of Wind Engineering and Industrial Aerodynamics* 95(9), 1259-1271.
- Caracoglia, L., Jones, N.P., 2007. Passive hybrid technique for the vibration mitigation of systems of interconnected stays. *Journal of Sound and Vibration* 307, 849–864.
- Caracoglia, L., Zuo, D., 2009. Effectiveness of cable networks of various configurations in suppressing stay-cable vibration, *Engineering Structures* 31(12), 2851–64.
- Li, F.C., Chen, W.L., Li, H., 2010. An ultrasonic transmission thickness measurement system for study of water rivulets characteristics of stay cables suffering from wind-rain-induced vibration. *Sensors and Actuators A: Physical* 159(1), 12-23.
- Li, S.Y., Zhong, W., 2013. Experimental study on the aerodynamic characteristics of stay cables with helical lines. *China Civil Engineering Journal* 46(7), 108-115. (in chinese).
- Li, S.Y., Zhong, W., 2014. Numerical simulation on the aerodynamic characteristics of stay cables with helical lines. *China Civil Engineering Journal* 27(4), 488-496. (in chinese).
- Olivier, F., 1995. Rain-wind induced vibration of cables. *Journal of Wind Engineering and Industrial Aerodynamics* 57, 353-362.
- Peil, U., Nahrath, N., 2003. Modelling of rain-wind induced vibration. *Wind and Structures* 6(1), 41-52.
- Reisfeld, B., Bankoff, S.G., 1992. Non-isothermal flow of a liquid film on a horizontal cylinder. *Journal of Fluid*

- Mechanics 236, 167-196.
- Robertson, A.C., Taylor, I.J., Wilson, S.K., 2010. Numerical simulation of rivulet evolution on a horizontal cable subject to an external aerodynamic field, *Journal of Fluids and Structures* 26, 50-73.
- Raftoyiannis, I.G., Michaltsos, G.T., 2016. Movable anchorage systems for vibration control of stay-cables in bridges, *Engineering Structures* 112, 162-171.
- Krenk, S., 2000. Vibration of a taut cable with an external damper, *Journal of Applied Mechanics ASME* 67 772–776.
- Cheng, S., Deravandi, N., Ghrib, F., The design of an optimal viscous damper for a bridge stay cable using energy-based approach, *Journal of Sound and Vibration* 329(22) (2010) 4689–4704.
- Verwiebe C., Ruscheweyh, H., 1998. Recent research results concerning the exciting mechanisms of rain-wind-induced vibrations. *Journal of Wind Engineering & Industrial Aerodynamics* 74–76(98), 1005-1013.
- Wei, J.D., Yang, Y.F., 2000. Analysis of cable vibration control using cross ties by finite element method, *China Journal of Highway and Transport* 13, 66-69. (in chinese).